## **CONFERENCE PRE-PRINT**

# IMPACT OF PLASMA BOUNDARY ON MACHINE OPERATION AND THE RISK MITIGATION STRATEGY ON JET

H.J. Sun

UKAEA (United Kingdom Atomic Energy Authority), Culham Campus, Abingdon, Oxfordshire, OX14 3DB, UK:

Email: HongJuan.Sun@UKAEA.uk

<sup>1</sup>P. Lomas, <sup>1</sup>G. Matthews, <sup>2</sup>M. Faitsch, <sup>1</sup>C Giroud, <sup>1</sup>D. King, <sup>2</sup>M Bernert, <sup>3</sup>E. Lerche, <sup>1</sup>FG. Rimini, <sup>2</sup>A. Kappatou, <sup>4</sup>N. Vianello, <sup>1</sup>J. Mailloux, <sup>5</sup>JET Contributors and <sup>6</sup>the EUROfusion Tokamak Exploitation team <sup>1</sup>UKAEA (United Kingdom Atomic Energy Authority), Culham Campus, Abingdon, Oxfordshire, OX14 3DB, UK; <sup>2</sup>Max Planck-Institute for Plasma Physics, Boltzmannstr. 2, D-85748 Garching, Germany; <sup>3</sup>Laboratory for Plasma Physics LPP-ERM/KMS, B-1000 Brussels, Belgium; <sup>4</sup>Consorzio RFX, Corso Stati Uniti 4, 35127 Padova, Italy; <sup>5</sup>See the author list of C. Maggi et al, 2024 Nucl. Fusion 64 112012; <sup>6</sup>See the author list of E. Joffrin et al, 2024 Nucl. Fusion 64 112019

#### **Abstract**

This study analyses separatrix and Scrape-off-Layer (SOL) characteristics in three JET scenarios: Quasi-Continuous Exhaust (QCE), ITER Baseline, and X-point Radiator (XPR). All aim to provide power exhaust solutions compatible with reactor operations. The QCE regime stands out for its higher separatrix and SOL collisionality, resulting in broader SOL widths. Combined with a near-double-null (DNX) configuration, this leads to operational challenges, including increased interaction with fast beam neutrals, elevated power loads on local limiters, and heat on Upper Dump Plate Tiles up to 5–6 times higher than other scenarios. Energy deposition also shows strong inner—outer asymmetry, with the outer limiter receiving up to four times more energy. Nevertheless, careful operational planning and robust real-time protection successfully managed these loads, enabling effective QCE operation. The QCE regime thus exemplifies the importance of integrating physics understanding, risk assessment, operational strategy, and real-time protection in developing new fusion scenarios.

### 1. INTRODUCTION

Over decades, fusion research has focused on developing plasma scenarios that ensure reliable, efficient tokamak operation, with candidates offering higher fusion power and longer pulses. Achieving reactor-compatible scenarios remains challenging, requiring optimization of power, energy gain, and component longevity while managing steady and transient power loads on plasma-facing components (PFCs).

JET has prioritized integrated, edge-compatible scenarios to address power exhaust issues, leveraging its flexibility and tritium-capable environment to provide insights relevant to ITER and next-step devices. This study examines three JET scenarios— Quasi-Continuous Exhaust (QCE)[1], ITER Baseline[2], X-point Radiator (XPR)[3], and—to analyze separatrix and Scrape-Off Layer (SOL) characteristics and their impact on machine operation.

The QCE regime achieves type-I ELM-free operation through strong plasma shaping, high separatrix density, and broad SOL profiles, relying on intrinsic plasma conditions rather than high impurity injection. Scaling QCE to JET highlights operational challenges such as higher heat loads on limiters and the upper dump plate, while providing valuable insights into reactor-relevant performance. The ITER Baseline scenario focuses on high confinement with partially detached divertor conditions, using neon or nitrogen seeding to manage heat loads and mitigate type-I ELMs. The XPR regime dissipates exhaust power through heavy impurity seeding to radiate energy before it reaches the divertor, enabling stable detachment and ELM suppression.

This paper uses QCE as a case study to illustrate risk identification, mitigation strategies, and successful operation, with ITER Baseline and XPR scenarios providing comparison. Subsequent sections present findings on SOL width, cross-field transport effects, and the role of operational planning and real-time protection in ensuring safe and effective scenario implementation for future fusion devices.

## 2. BROADER SOL WIDTH IN QCE REGIME

QCE employs strong shaping to suppress type-I ELMs, using a near-DN shape with vertical inner and horizontal outer strike points, as shown in figure 1. The JET-ITER-Baseline scenario uses high triangularity with both strike points on vertical targets, matching ITER. XPR has low triangularity with the same divertor geometry.

In figure 2, the near SOL density decay length,  $\lambda_{n_e}$  is normalized using the poloidal gyro-radius,  $\rho_{s,pol} = \frac{\sqrt{m_i T_{e,sep}}}{e B_{pol}}$  and plotted against normalized SOL collisionality  $v_{SOL,e}^* \approx \frac{10^{-16} n_{e,u} L}{T_{e,u}^2}$  to illustrate the change of SOL profiles. Here, the separatrix density,  $n_{e,u}$ , is taken at the point where  $T_{e,u} \approx 100$  eV and the connection length  $L = \pi q_{95} R$ . QCE pulses exhibit much broader SOL widths, with both  $\lambda_{n_e}$  up to three times at high  $v_{SOL}^*$  compared to the pulses from other two scenarios, consistent with previous AUG [4] and JET [5] results.

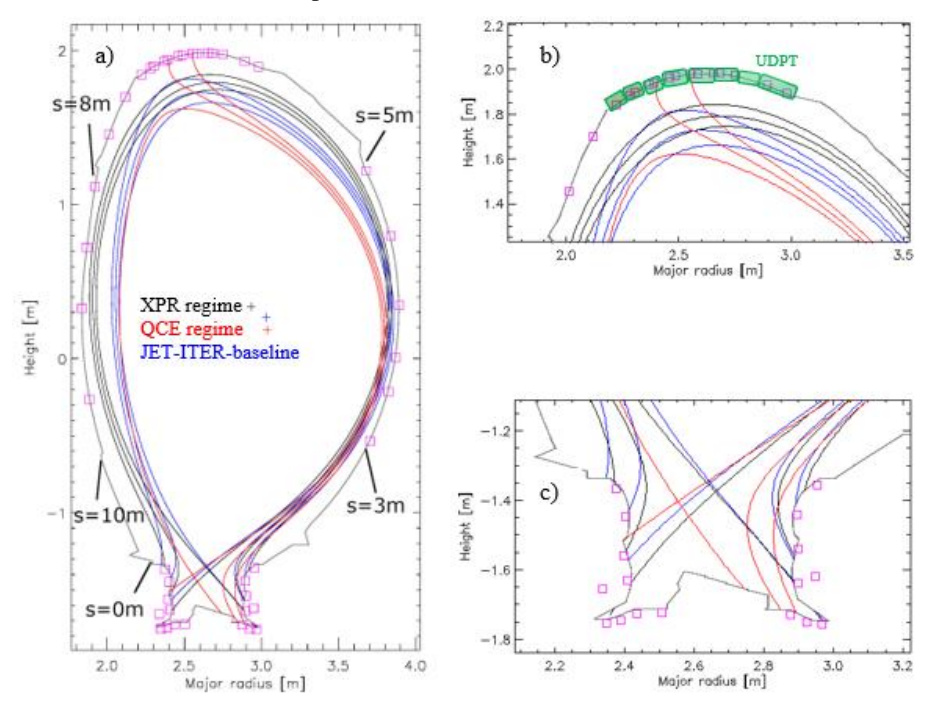
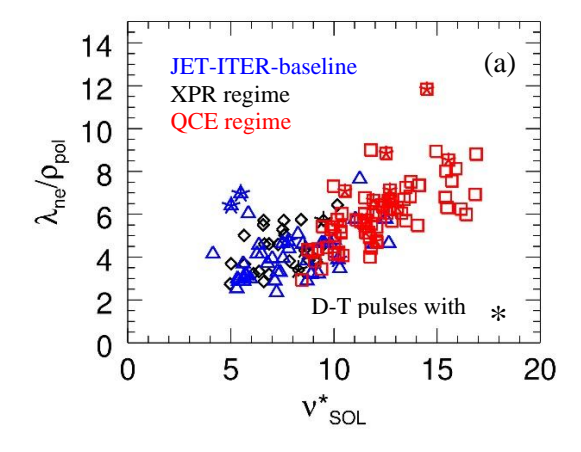


Figure 1. Poloidal cross-sections of JET-ITER-baseline #102787 (blue), XPR #102719 (black), and QCE #102902 (red): (a) full plasma, (b) upper plasma, and (c) divertor. Magenta squares indicate thermocouples; sss in (a) is the poloidal distance along the first wall. UDPT are shown schematically as green boxes in (b)

Figure 2b replotted the data against  $\alpha_t = 3 \cdot 10^{-18} R q_{cyl}^2 \frac{n_u}{T_u^2} Z_{eff}$ , broadly consistent with AUG results [6], though QCE shows scattered trends. Comparing figure 2a and 2b,  $v_{SOL}^*$  appears to be a better ordering parameter across the dataset. However, the form  $v_{SOL}^*$  was originally derived under the assumption that  $Z_{eff} \approx 1$  in (Stangeby, 2000). For JET non-seeded pulses as in the pure tritium dataset and QCE pulses with small to intermediate amount of neon ( $c_{Ne} < 1\%$ ), this assumption may hold as they have relatively small derivation from the assumption  $Z_{eff} \approx 1$ . However, in ITER-baseline and XPR regimes,  $Z_{eff}$  can reach up to 3 and varies significantly with impurity species and seeding levels, making the assumption no longer valid.

Given that the separatrix position in the  $v_{SOL}^*$  calculation is assumed as at  $T_{e,u} \approx 100$  eV, the parameter can be further simplified as  $v_{SOL,e}^* \approx \frac{10^{-16}n_{e,u}L}{T_{e,u}^2} = 10^{-20}n_{e,u}L$ . To avoid confusion,  $n_{e,u}L$  is used in the rest of paper instead of  $v_{SOL}^*$  when relating the separatrix and SOL characteristics to JET operational issues.



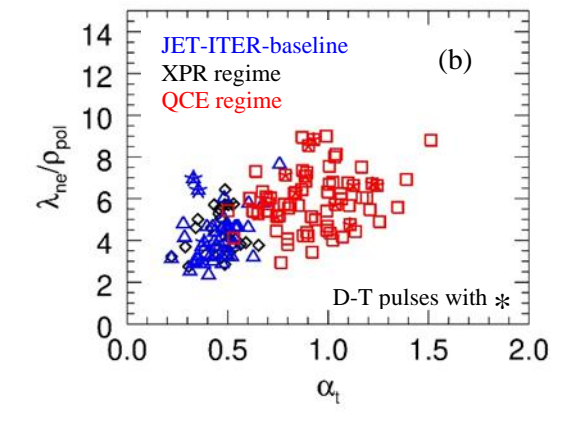


Figure 2. (a) The near SOL density decay length,  $\lambda_{n_{e,u}}$ , normalized to the  $\rho_{s,pol}$  against  $\nu_{SOL}^*$ . (b) The near SOL density decay length,  $\lambda_{n_{e,u}}$ , normalized to the  $\rho_{s,pol}$  against the turbulence control parameter  $\alpha_t = 3 \cdot 10^{-18} Rq_{cyl}^2 \frac{n_u}{T_u^2} Z_{eff}$ . Blue triangles are ITER-Baseline pulses, black diamonds are XPR pulses, and red squares are QCE pulses, D-T pulses are marked with an additional asterisk.

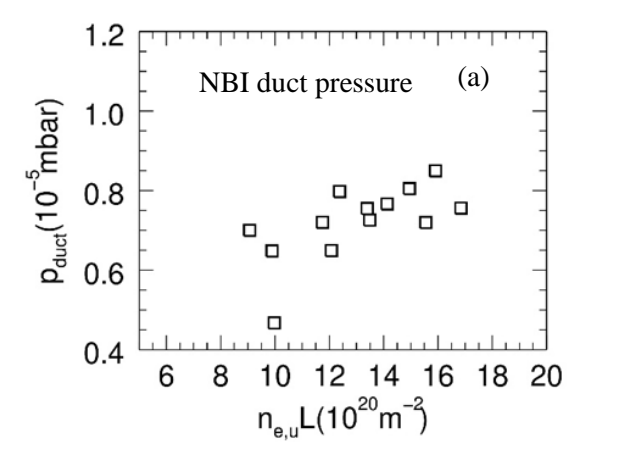
## 3. Impact of QCE plasma boundary on JET operation

## 3.1. Interaction with NBI: duct pressure and re-ionisation issue

Neutral Beam Injection (NBI) is a primary heating method on JET. The vessel is divided into eight octants, with injector boxes in Octants 4 and 8, each containing eight PINIs. Injected neutrals are ionised in the plasma, and the resulting fast ions heat the bulk plasma via Coulomb collisions. Some neutrals are re-ionised in the beam ducts by background gas, depositing power on in-vessel components. Since the ionisation rate scales with duct pressure, Penning gauges monitor it, and NBI is shut down if pressure exceeds  $1.2 \times 10^{-5}$  mbar to avoid excessive power load

Elevated duct pressures were seen in QCE pulses, limiting the total fuelling for the experiment [1]. Figure 3a shows pressures rising with  $n_{e,u}L$ .; two high-density pulses had reduced pressures because two PINIs were shut down by the Real time control system. Later, neon seeding was used to control duct pressure by reducing SOL density and particle flux and became standard in QCE operation.

Re-ionisation can also occur near the duct exit and in the SOL region, posing melting risk to the local Be limiter. In the earlier tritium campaign, enhanced SOL broadening increased particle flux, producing excessive power loads[7]. A similar issue was observed in QCE pulses. Figure 3b shows Be wall surface temperature data: Wall overheating did not correlate with NBI power, but instead with the SOL density decay length  $\lambda_{ne,u}$ , confirming enhanced cross-field transport raises re-ionisation and limiter heat loads. Most QCE pulses stayed below 850 °C as the cases with higher temperature were terminated early by Real Time Protection System.



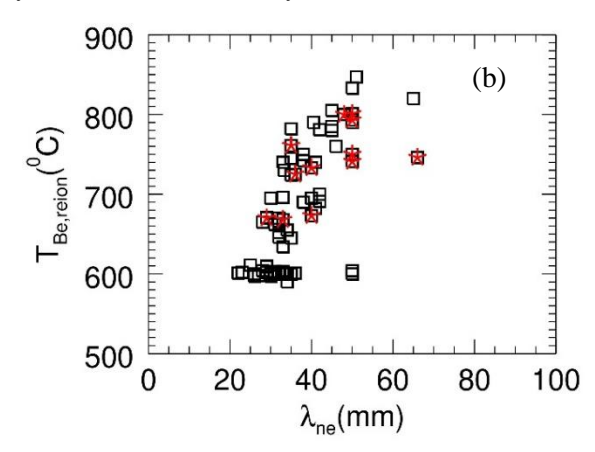


Figure 3 (a) NBI O duct pressure against  $n_{e,u}L$ , for QCE non-neon seeding pulses. (b) Surface temperature  $T_{Be,wall}$  of the limiter next to NBI Octant 4 duct measured by a near-IR camera caused by re-ionisation issue against near SOL density decay length  $\lambda_{n_{e,u}}$  for QCE pulses.

#### 3.2 Impact on energy distribution to PFCs

PFC loads were assessed using near-IR cameras and tile calorimetry [8]. Divertor target losses were excluded, as each scenario employs distinct exhaust solutions under separate studies. In QCE, the DNX configuration with vertical inner and horizontal outer strike points complicates direct comparison with ITER-baseline and XPR, which both use vertical—vertical geometry. However, thermocouples are not available on the QCE outer strike target tiles, preventing reliable total energy measurements at the target.

On JET, broader SOL widths and DNX geometry in QCE pulses significantly enhance main-chamber and UDPT loads. Figure 4a shows energy densities  $\sim 3 \times$  higher on the outer limiter and  $5-6 \times$  higher on the UDPT than in ITER-baseline and XPR pulses, despite similar input energies ( $\sim 170$  MJ). Inner limiter loads are higher overall than in reference pulse #89953 [8] due to additional NB shine-through, though scenario differences there are modest.

For most JET-ITER-baseline and XPR pulses, energy losses to the UDPT increase linearly with total radiation, except for a few D-T pulses. QCE pulses exhibit higher overall energy deposition on the UDPT, and the relationship with total radiation is non-linear, suggesting that sources in addition to radiation, such as SOL plasma, contribute to the energy measured on the UDPT. This is demonstrated in figure 4b, where the normalized energy

on the UDPT, relative to total radiated energy, increases with  $n_{e,u}L$  for QCE pulses. For JET-ITER-baseline and XPR pulses, across a broad range of  $n_{e,u}L$  values, the energy ratio on the UDPT to total radiation remains relatively constant, indicating that energy losses primarily originate from radiation, with minimal contribution from SOL plasma. The extra energy load observed in QCE pulses mainly arises from the DNX configuration used in the QCE regime, where a fraction of the parallel transport in the SOL reaches the UDPT and deposits energy there.

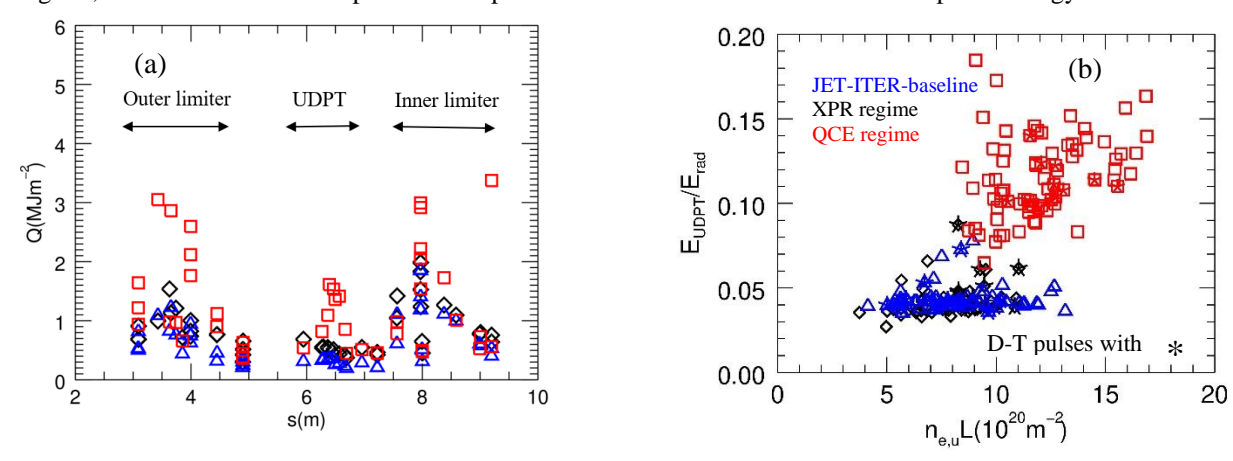


Figure 4. (a) Pulse-averaged energy density derived from tile calorimetry against the distance along the first wall poloidally, for ITER-Baseline pulse #102664 (blue triangles), for XPR pulse #102719 (black diamonds), and QCE pulse #104495 (red squares (b) The normalized energy found on UDPT by total radiated energy against  $n_{e,u}L$ . D-T pulses are marked with an additional asterisk.

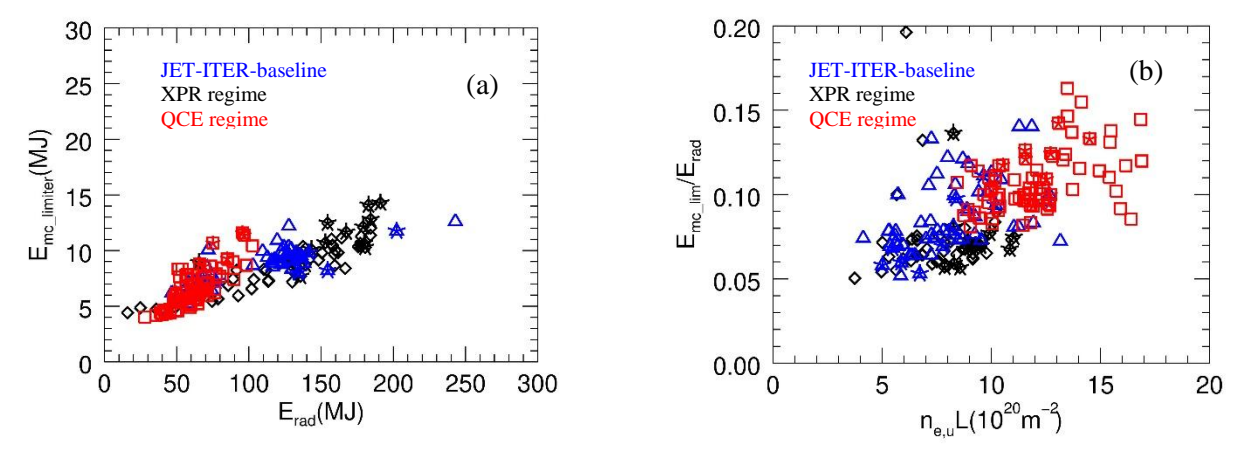


Figure 5. a) Energy losses to main chamber limiters by tile calorimetry against total radiation; (b) The normalized energy found on main chamber limiters by total radiated energy against  $n_{e,u}L$ . D-T pulses are marked with an additional asterisk.

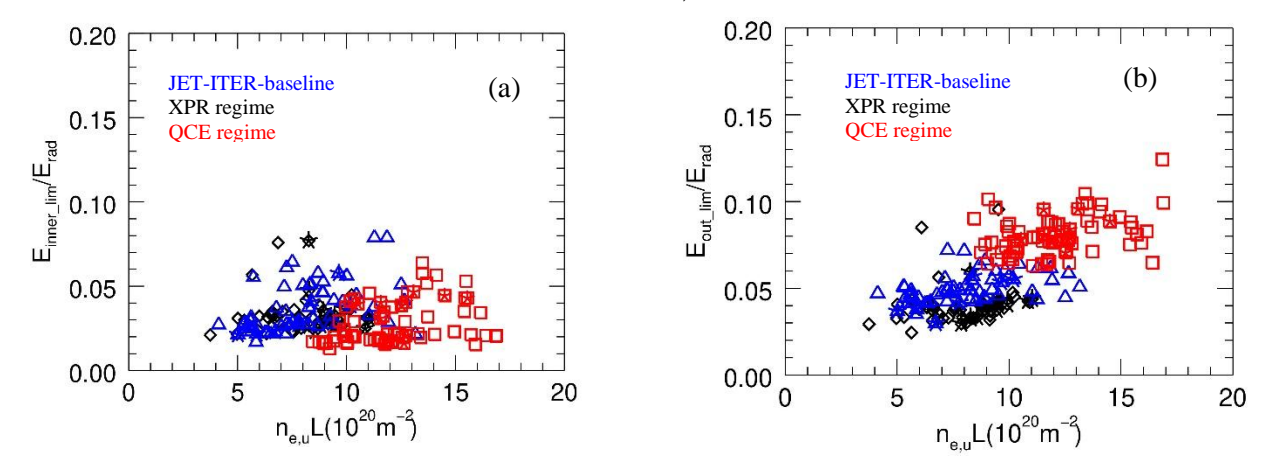


Figure 6. a) The normalized energy to inner limiters by total radiated energy against  $n_{e,u}L$ . (b) The normalized energy to outer limiters by total radiated energy against  $n_{e,u}L$ .

Analysis of selected pulses shows limiter energy losses generally scale with total radiation, but at a much higher rate for QCE pulses (figure 5a). Limiter loads arise from plasma radiation and SOL transport: if radiation dominates, the deposited-to-radiated energy ratio should remain constant; if SOL transport contributes, correlations with SOL parameters are expected. Normalizing deposited energy by total radiation and plotting against  $n_{e,u}L$  (figure 5b) shows a nearly constant 5–7% for JET-ITER-baseline and XPR pulses, with a modest rise aboven<sub>e,u</sub>L > 8. By contrast, most QCE pulses display a clear increase, indicating stronger SOL transport contributions. Some baseline pulses show higher fractions due to NBI shine-through.

Figure 6 separates inner and outer limiter loads. QCE pulses deliver significantly more energy to outer limiters—typically 3–4 times higher than inner—while the inner share shows no consistent trend. XPR pulses exhibit the most symmetric distribution, whereas baseline pulses deposit about twice as much on the outer limiter. This asymmetry reflects plasma shape: XPR has balanced inner/outer gaps, while baseline and QCE configurations feature larger inner gaps that spread radiation beyond accounted regions. In QCE, the near-DNX geometry also diverts part of the SOL power to the UDPT, further increasing outer limiter loads.

4. The risk mitigation strategy on JET

#### 4.1 Scenario Development strategy

The last near-DNX experiments with auxiliary heating were in 2006 with a CFC wall; in 2020 the shape was tested once in Ohmic conditions with the Be–W wall. As JET was not designed for DNX and the UDPT cannot sustain high loads, overheating risk was the main concern. Considerable efforts were dedicated to operational planning to mitigate any potential damage.

The desired configurations across various plasma current ranges were derived from historical reference pulses using the plasma equilibrium Code - Proteus. During the design phase, a proximity scan of the plasma separatrix to the UDP was conducted in Proteus for each configuration. This assessment aimed to determine the maximum permissible power to the upper outer divertor leg. Figure 7 illustrates the relationship between the maximum allowed power and the distance from the separatrix to the UDP.

When the experiment was executed, a progressive and stepwise approach was planned and performed:

- Step 1: Verifying the designed DNX configuration. The initial test used a 1.5 MA Ohmic pulse to verify the DNX configuration. In the first shot (#101819), visible cameras showed signs of UDP overheating, leading to a revised pulse with improved top-gap control.
- Step 2: Assessing the UDPT power handling. To assess potential degradation of the UDP after a decade of operation, a high-triangularity 10 MW pulse—previously run in the early ILW phase (#82484, 2012)—was repeated. The top gap was reduced from a large initial value to the reference level while monitoring control accuracy. Results showed that the UDP Be tiles retained power handling comparable to their 2012 condition.
- Step 3: Implementing DNX with auxiliary heating. The DNX configuration with auxiliary heating began at ≈10 MW and a large top clearance. Heating power, DNX duration, and fuelling were then gradually increased while reducing the top gap, with each step contingent on the absence of excessive loads or UDP overheating.

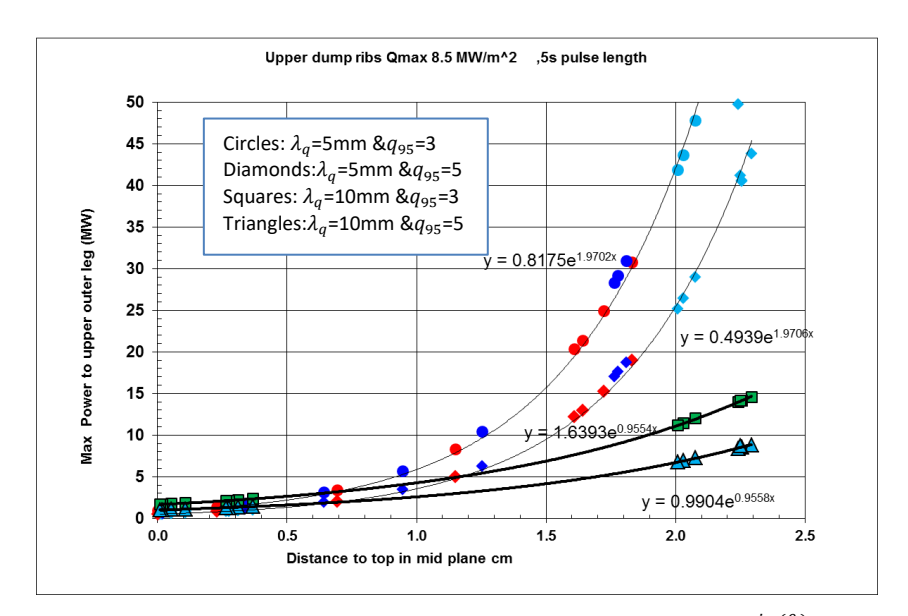


Figure 7. Maximum allowable power for QCE, calculated by  $(1 - F_{rad})f_{UP}P_{in} = Q^{max}\frac{\sin{(\theta,)}}{\sin{(\theta,+\alpha)}}A_{\lambda}$ , where  $Q^{max}$  is max allowed power density on Be limiter, 8.5 MWm<sup>-1</sup>;  $F_{rad}$  is radiation fraction (empirically 30%) and  $f_{UP}$  is the fraction of the power directed to the upper divertor (1/3 assumed); tile chamfer angle  $\alpha = 13^{\circ}$ ; the perpendicular field line angle  $\theta_{\lambda}$  and.  $A_{\lambda}$  are calculated by Proteus.

## **4.2 Robust real time protection**

JET has developed a robust and sophisticated real-time protection system to ensure machine integrity. The deployment of the scenario development strategy for the QCE regime cannot be fulfilled without JET's comprehensive real-time protection system. However, the overall framework of JET's protection system is complex, and an overview paper on the protection systems is planned for the near future. Here, the most relevant elements for QCE scenario development that protect against high PFC power loads are introduced.

A real-time imaging protection system monitors PFCs using CCD cameras, covering the majority of PFCs and integrating with the main tokamak controls and heating systems. This imaging system consists of eleven analogue CCD cameras, which demonstrate high robustness against changes in system parameters such as emissivity. The system monitors about two-thirds of the main chamber wall and almost half of the divertor. A real-time image processing unit converts raw data into surface temperatures, accounting for varying material emissivity and correcting artifacts caused by neutron impact. Regions of interest (ROI) on selected PFCs are analysed in real-time, and the maximum temperature for each ROI is sent to other real-time systems to trigger appropriate plasma control responses based on hotspot locations.

During QCE experiment, detection of high temperatures in either the re-ionisation region or UDPT triggers a tailored response. Figure 8a provides an example (#102095) of such an event: when the UDPT Be surface temperature rises past the 925°C threshold and remains above it for more than 200ms, the protection system triggers a tailored response. This response consists of a number of actions all aimed at reducing the power loading on the UDPT: it immediately turns off NB heating to prevent further overheating, reduces plasma current to lower thermal and magnetic energy, maintains ICRH at 1.5 MW for 1.5 s to avoid radiative disruption, and increases both the top gap (TG) and radial outer gap (ROG) to distance the plasma from PFCs.

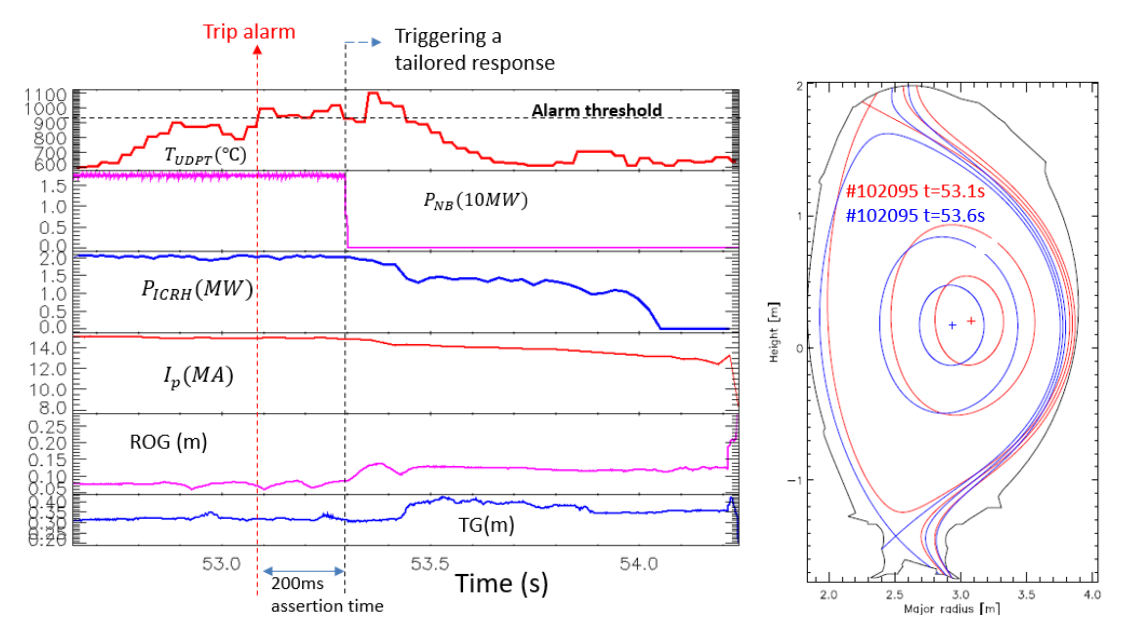


Figure 8. (a) Time traces of an example #102095 triggered by a hotspot in UDPT. (b) Configurations before and after the hotspot alarm.

As shown in figure 8b, the overheating was primarily caused by the configuration inadvertently shifting to an upper null X-point shape during a top gap scan attempt. When the hotspot alarm was triggered, the configuration switched to a safer shape: lower single null, low triangularity, and slim, to minimize forces on the vessel in the event of a disruption. As shown in figure 8a, the surface temperature of the UDPT continues to increase even after the NBI heating is turned off. This is because the temperature rise is primarily driven by interaction with the hot plasma, not by direct NBI heating. Since adjusting the plasma shape takes tens of milliseconds, the surface temperature keeps rising during this delay. This is the main reason the alarm threshold is set below the Beryllium melting point of 1287°C. The pulse eventually disrupted at 54.2 s, but with significantly reduced energy, avoiding damage to the UDPT. For subsequent pulses, the TG was increased to prevent similar incidents.

A complementary real-time monitoring system, known as WALLS, uses thermal models of the plasma to evaluate the wall surface temperature. It also monitors the plasma boundary geometry, ensuring the plasma does not enter prohibited configurations that could directly expose the wall to the plasma—a critical feature for the development of new scenarios like QCE. Figure 9 provides such an example (#101885): WALLS trips an alarm because the gap between separatrix and UDPT was too small, despite the surface temperature remaining below alarm threshold. The plasma was subsequently shifted to a safe shape as in #102095 and the plasma terminated in a controlled manner without causing any damage to the PFCs.

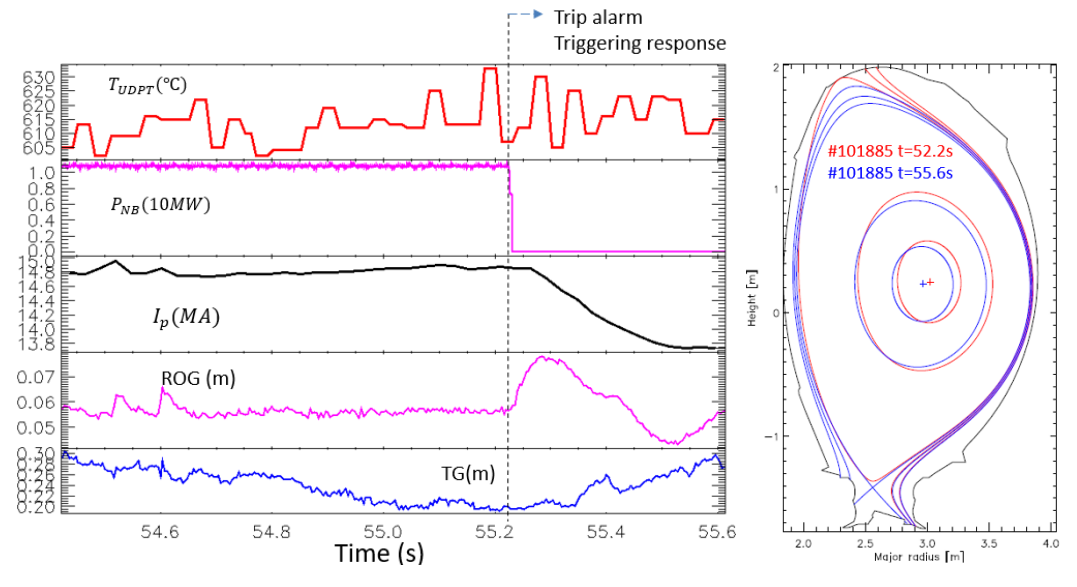


Figure 9. (a) Time traces of an example #101885 triggered by WALLs top gap. (b) Configurations before and after the gap alarm.

In addition to the real-time protection system, JET has implemented real-time network to enhance sicentific outcomes while maintaining the integrity of the device. Here, those important during scenario development for QCE regime are introduced. The plasma will be terminated once it is tripped on alarm like re-ionisation hotspot or NBI duct pressure limit. While this approach effectively protects the PFCs from damage of NBI re-ionisation, the plasma often results in terminating prematurely and the scientific productivity is limited. The in-situ real-time network is designed to address this issue to optimize the scientific outcomes. Instead of terminating the plasma, the network temporarily switches off one or two PINIs when wall surface temperature or NBI duct pressure approaches alarm thresholds. Once these parameters drop below a certain level, the PINIs are switched back on. This dynamic adjustment allows for continued operation and reliable scientific results, despite minor fluctuations in heating power. The Plasma Termination Network (PTN) always remains active to ensure safety of the machine so, if these actions do not sufficiently mitigate PFC heating or duct pressure rise, the usual simple termination will still be triggered.

### 4. SUMMARY AND DISCUSSION

This study investigates how plasma boundary characteristics affect JET operations and emphasizes the need for integrated scenario development. Three scenarios were assessed—the QCE regime, the JET-ITER-Baseline, and the XPR regime—each providing different approaches to power exhaust. The QCE regime, characterized by broad SOL profiles and strong plasma shaping, posed the greatest operational challenges but was successfully executed through thorough preparation and advanced protection systems.

Prior knowledge from AUG, TCV, and earlier JET campaigns informed planning. Anticipated risks included enhanced NBI re-ionisation near the duct, elevated fluxes to main chamber limiters, and increased loads on the UDP tiles. Mitigation strategies combined Proteus modelling of plasma—wall gaps, stepwise operational approaches, increased neon seeding, and advanced real-time controls. The CCD-based PFC monitoring system and the WALLS thermal model enabled active management of overheating, ensuring safe operation.

The broadened SOL profiles in QCE increased limiter and wall loading but also distributed power more widely, reducing stress on the divertor target—an effect consistent with AUG observations [9]. Although diagnosing the far SOL remains difficult, correlations between separatrix parameters and limiter loads suggest potential for new models and diagnostics, provided overheating risks are controlled.

Overall, the QCE experiments highlight how combining physics insight, risk identification, and robust protection systems enables safe exploration of advanced scenarios [1][10]. The findings deepen understanding of plasma boundary behaviour and provide a framework for scenario development in future fusion reactors.

#### **ACKNOWLEDGEMENTS**

This work has been carried out within the framework of the EUROfusion Consortium, funded by the European Union via the Euratom Research and Training Programme (Grant Agreement No 101052200 — EUROfusion) and from the RCUK [grant number EP/T012250/1]. Views and opinions expressed are however those of the author(s) only and do not necessarily reflect those of the European Union or the European Commission. Neither the European Union nor the European Commission can be held responsible for them. This work has been (part-) funded by the EPSRC Energy Programme [grant number EP/W006839/1]. To obtain further information on the data and models underlying this paper please contact PublicationsManager@ukaea.uk\*.

## REFERENCES

- [1] M. Faitsch et al, Nuclear Fusion, vol. 65, p. 024003, 2025.
- [2] C. Giroud et al, Nuclear Fusion, vol. 64, p. 106062, 2024.
- [3] M. Bernert et al, Nuclear Materials and Energy, vol. 43, p. 101916, 2025.
- [4] H. J. Sun et al, Plasma Phys. Control. Fusion, vol. 57, p. 125011, 2015.
- [5] H. J. Sun et al, Nucl. Fusion, vol. 61, p. 066009, 2021
- [6] T. Eich et al, Nucl. Fusion, vol. 60, p. 056016, 2020.
- [7] H. Sun et al, Nuclear Fusion, vol. 63, p. 016021, 2023.
- [8] G. Matthews et al, Nuclear Materials and Energy, vol. 12, pp. 227-233, 2017
- [9] A. Redl et al, Nucl. Fusion, vol. 64, p. 086064, 2024.
- [10] H. Sun et al, Nuclear Fusion, vol. 65, p. 076012, 2025